Bubble Morphology in U_3Si_2 Implanted by High-Energy Xe Ions at 300°C

Yinbin Miao[a,*], Jason Harp[b], Kun Mo[a], Shaofei Zhu[a], Tiankai Yao[c], Abdellatif M. Yacout[a]

[a]*Argonne National Laboratory, Lemont, IL 60439, United States*
[b]*Idaho National Laboratory, Idaho Falls, ID 83415, United States*
[c]*Rensselaer Polytechnic Institute, Troy, NY 12180, United States*

Abstract

The microstructure modifications of a high-energy Xe implanted U_3Si_2, a promising accident tolerant fuel candidate, were characterized and are reported upon. The U_3Si_2 pellet was irradiated at Argonne Tandem Linac Accelerator System (ATLAS) by an 84 MeV Xe ion beam at 300°C. The irradiated specimen was then investigated using a series of transmission electron microscopy (TEM) techniques. A dense distribution of bubbles were observed near the range of the 84 MeV Xe ions. Xe gas was also found to accumulate at multiple types of sinks, such as dislocations and grain boundaries. Bubbles aggregated at those sinks are slightly larger than intragranular bubbles in lattice. At 300°C, the gaseous swelling strain is limited as all the bubbles are below 10 nm, implying the promising fission gas behavior of U_3Si_2 under normal operating conditions in light water reactors (LWRs).

Keywords: silicide fuels, fission gas behavior, ion irradiation, light water reactor (LWR), microstructure characterization

1. Introduction

Development of new fuel-cladding solutions with enhanced accident tolerance so as to replace currently dominant UO_2-zirconium solution in light water reactors (LWRs) has been the focus of nuclear materials community since the tragic nuclear accident in Fukushima Daiichi Nuclear Power Plant [1, 2]. The fuel materials satisfying the qualifications of accident tolerant fuels

*Tel: +1 (630)252-7448. Email: ymiao@anl.gov (Y. Miao)

(ATFs) are expected to be compounds or alloys of uranium that have two advantages over UO_2: higher thermal conductivity and higher heavy metal density. The former advantage ensures a lower stored energy during normal operation as well as fast removal of decay heat under accident conditions, whereas the latter one leads to extra neutronics benefits that may either provide more flexibility in the selection of ATF cladding materials or increase economic profits for utilities. Therefore, with both advantageous features discussed above [3], U_3Si_2 has been regarded as a promising ATF candidate and thus attracting intense attention from the nuclear materials community [4, 5, 6, 7, 8].

In order to validate U_3Si_2 as a qualified LWR fuel material, its fuel performance must be comprehensively understood through systematic investigations. However, as a fuel material that has been successfully applied in research reactors to reduce uranium enrichment, previous experimental and modeling efforts on U_3Si_2 have been concentrated on low-temperature research reactor conditions [9, 10, 11, 12, 13]. Namely, there only exist a limited number of references that involves fuel performance of U_3Si_2 under LWR conditions [4, 7]. At typical research reactor temperatures (< 250°C), U_3Si_2 loses its crystalline structure at merely 0.3 dpa and keeps amorphous throughout the remainders of fuel life [14]. On the other hand, at LWR temperatures ($\geq$ 300 °C), U_3Si_2 tends to maintain its tetragonal lattice structure under irradiation [7]. The first results from the U_3Si_2 irradiation test discussed in Ref. [5] are currently being generated. Initial neutron radiography indicates that the pellets are largely intact and no run-away swelling was observed at a fission density of approximately 6×10^{20} fissions/cm^3 [15]. Therefore, the U_3Si_2 materials in research reactors and in LWRs are literally in two different phases, and hence subject to have significant dissimilarity in fuel behavior. In this regard, it is insufficient to solely rely on research reactor data of U_3Si_2 to evaluate its qualifications as a LWR fuel material.

Gaseous fission products are generated during fission reactions, and accumulate to form intragranular and intergranular bubbles in nuclear fuels. By causing gaseous swelling and originating fission gas release, those fission gas bubbles significantly contribute to the degradation of fuel performance. Thus, establishing comprehensive understanding of fission gas behavior in U_3Si_2 under LWR conditions is crucial to the determination of this material as an ATF. Unfortunately,

this effort is obstructed by the absence of experimental investigations of bubble evolution in U_3Si_2 at LWR temperatures. Although the in-pile irradiation experiments of U_3Si_2 have been in progress as a part of the ATF-1 irradiation campaign in Advanced Test Reactor (ATR) [16, 5], the detailed post-irradiation experiment (PIE) data will not be available to the ATF community for a while considering the time-consuming and costly nature of PIE on in-pile irradiated fuel materials. Hence, it is of great value to utilize ion irradiation as an inexpensive and timely alternative to study fission gas behavior in U_3Si_2. Being capable of creating various neutron-induced microstructure modifications, ion irradiation has been extensively used to study radiation effects in materials [17, 18, 19]. More importantly, the ~100 MeV fission fragments, which cause the majority of microstructure modifications in nuclear fuels, can be replicated by the high-energy ion irradiation technique [20]. In this study, the high-energy ion acceleration capability of Argonne Tandem Linac Accelerator System (ATLAS) [21] was utilized to implant Xe, the most important and representative gaseous fission product, into U_3Si_2 material at a LWR temperature so that the fission gas behavior in U_3Si_2 under normal LWR operating conditions can be unveiled prior to the availability of in-pile irradiation PIE data.

2. Experiments

2.1. Sample Preparation

The U_3Si_2 pellet used in this study was manufactured at Idaho National Laboratory [5]. The mixture of 92.5 wt% fine uranium powder and 7.5 wt% fine silicon powder was pressed at 225 MPa before being melted to produce ingots of U_3Si_2 compound. Those arc-melted ingots were then comminuted into fine powder. The U_3Si_2 fine powder was cold pressed and sintered into fuel pellets in an Ar protection atmosphere. The U_3Si_2 pellet used in this study was fabricated using the same procedures as for the pellets irradiated in ATR for the ATF-1 campaign [16]. More details about the pellet fabrication are described in Ref. [5]. Previous investigations of as-fabricated U_3Si_2 pellets indicate that the cold pressing and sintering technique introduces USi and UO_2 precipitates that comprise approximately 14% volume fraction. The pellet was cut into 3 mm thick discs with an 8.3 mm diameter for the ion irradiation experiment. The surface

exposed to ion irradiation was first mechanically polished to 0.05 micron surface roughness and then vibratory polished to reach its final surface finishing.

2.2. *Ion Implantation*

The high-energy ion irradiation experiment was performed at ATLAS facility, Argonne National Laboratory. An irradiation chamber was designed and established after the PII Linac of ATLAS. At this position, ATLAS is capable of accelerating heavy ions up to approximately 1 MeV/amu [21]. The disc specimen was adhered to a copper sample holder using PELCO high performance silver paste. A HeatWave Labs TB-175 cartridge heater that can heat the sample up to 1200°C was mounted on the back of the copper sample holder. The heater was powered by a DC power supply controlled by a proportional-integral-derivative (PID) controller. The temperature of the specimen was increased to 300°C and irradiated by 84 MeV Xe ions. This irradiation temperature is within LWR fuel temperature range, which is similar to the fuel surface temperature in boiling water reactors (BWRs). The temperature of the specimen slightly fluctuated several times when the ion beam was interrupted, whereas the PID controller managed to limit the temperature fluctuation, and maintain the specimen temperature within a range between approximately 290°C and 330°C. The energy of Xe ions is close to that of fission products and is therefore expected to produce similar microstructure modifications. The Xe beam profile was measured and centered by a Faraday cup. The beam current was maintained at approximately 100 particle nA for 20 hours. Assuming a 2D Gaussian beam shape, the peak ion fluence is approximately 1.38×10^{17} ions/cm^2. According to the SRIM simulation [22] following Stoller et al.'s method [23] (see Figure 1(b)), near the center of the specimen, the peak irradiation dose is 499 dpa, which occurs in a depth of ~6 μm to the surface. Meanwhile, the average Xe fraction from 5 micron to 8 micron from the surface is approximately 0.92%, which is equivalent to a 6.36%FIMA (fissions per initial metal atom).

2.3. *Characterization of the Irradiated Specimen*

The PIE characterization of the Xe-implanted U_3Si_2 specimen was carried out at the Materials Characterization Suite (MaCS) at Center for Advanced Energy Studies (CAES). A transmission

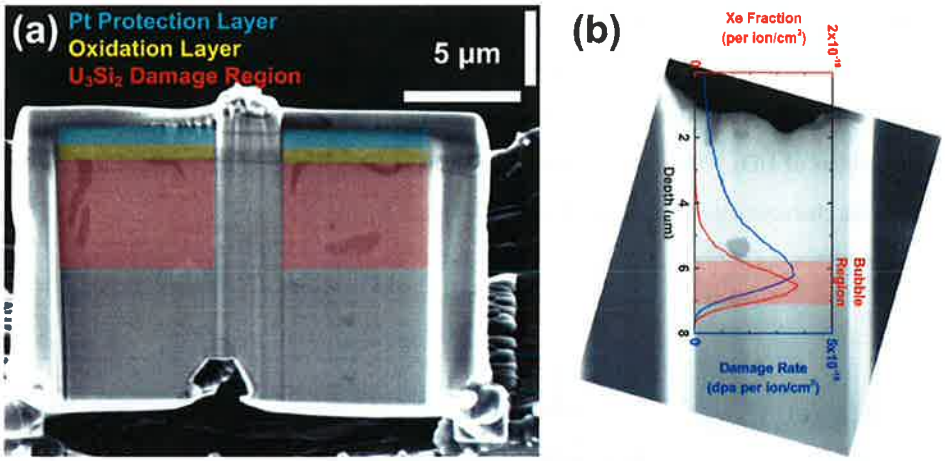

Figure 1: Overview of the regions influenced by the 84 MeV Xe ions: (a) a SEM image of the irradiated specimen showing both the thin oxidation layer and the remainder of the irradiation damage region of U_3Si_2; (b) a STEM HAADF Z-contrast image of the TEM foil overlaid with the SRIM prediction of the irradiation damage profile; the TEM foil was prepared by further thinning the irradiated specimen shown in (a).

electron microscopy (TEM) foil was lifted out (see Figure 1(a)) from the center of the irradiated specimen and thinned to approximately 75 nm (see Figure 1(b)) using an FEI Quanta 3D FEG focused ion beam (FIB). Then the TEM foil was investigated by an FEI Tecnai TF30-FEG STwin STEM working at 300 kV. Both TEM bright field (BF) and scanning transmission electron microscopy (STEM) high-angle annual dark field (HAADF) imaging techniques were utilized to examine the microstructures in the specimen, especially those Xe bubbles. Additionally, STEM-based energy dispersive X-ray spectroscopy (EDS or EDX) was used to analyze the element compositions of various phases in the specimen.

3. Results

3.1. Phases Identification

As previously reported by the manufacturers of the U_3Si_2 [5], two intrinsic secondary phases, USi and UO_2, coexist with the U_3Si_2 matrix in the fuel pellet in this study. After Xe implantation, those secondary phases were observed to remain in the specimen as indicated by Marks 3 and 4 in Figure 2(a). In comparison to the U_3Si_2 matrix (Figure 2(c)), the EDS analysis of the Mark

3 precipitate (Figure 2(g)) clearly shows the existence of extra Si, which is consistent with the element composition of USi. On the other hand, the EDS analysis of the Mark 4 precipitate (Figure 2(h)) illustrates the enrichment of O and depletion of Si, which implies the element composition of UO_2. The electron diffraction pattern (DP) of the Mark 4 precipitate further shows the characteristic [001] zone DP of UO_2 (Figure 2(b)).

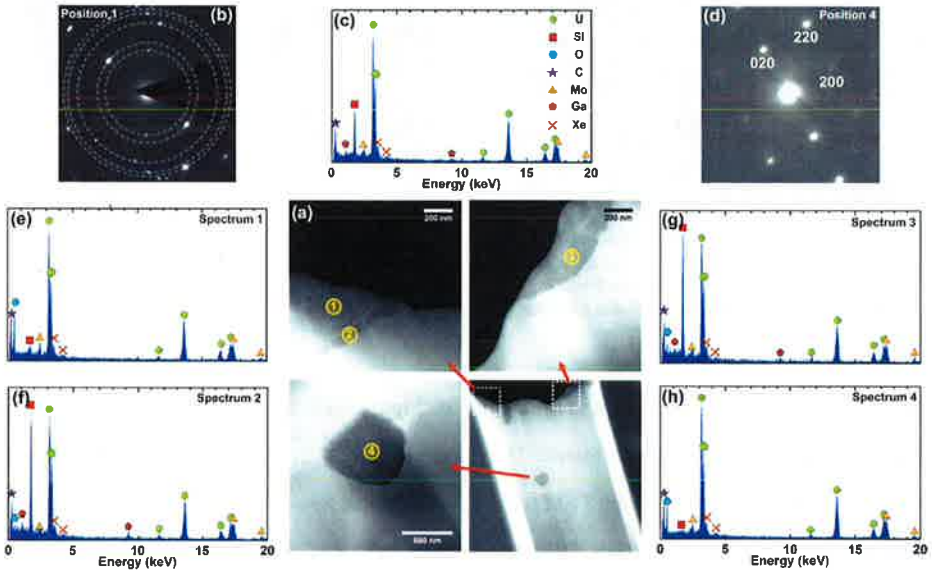

Figure 2: Phase analysis of the 84 MeV Xe implanted specimen: (a) STEM HAADF images showing multiple regions of interest (Spectra 1 through 4) investigated by EDS analysis; (b) electron diffraction pattern of the residual oxide layer (corresponding to Spectrum 1); dashed rings indicate the position of {111}, {200}, {220}, {311}, and {222} reflections of UO_2, respectively; (c) EDS profile of the matrix phase showing the dominant U and Si peaks of U_3Si_2 along with traceable Xe peaks; (d) electron diffraction pattern of a UO_2 precipitate (corresponding to Spectrum 4) showing the [001] zone of UO_2; (e) EDS profile of the oxide layer (Spectrum 1) showing the dominant U and O peaks; (f) EDS profile of the transition layer between the oxide layer and matrix (Spectrum 2) showing the dominant U and Si peaks; (g) EDS profile of a USi precipitate (Spectrum 3) showing the dominant U and Si peaks; (h) EDS profile of a UO_2 precipitate (Spectrum 4) showing the dominant U and O peaks. All Mo signals come from the Mo Omniprobe grid used to mount the TEM foil.

Aside from the intrinsic secondary phases, high-temperature ion implantation also facilitated the formation of an approximately 1 micron thick oxidation layer (see Mark 1 in Figure 2(a)). As previous observed in the *in situ* TEM ion irradiation investigation of U_3Si_2 [7] and reported in the *ex situ* ion irradiation experiments of Ce_3Si_2 [24], a non-radioactive surrogate of U_3Si_2, U_3Si_2 is readily to be oxidized under irradiation, even in a $\sim 10^{-5}$ Pa vacuum in TEM chamber.

In this study, the vacuum level during Xe implantation was approximately 10^{-4} Pa. Hence, it is expected that surface oxidation would occur. The oxidation layer shows an EDS profile (Figure 2(e)) very similar to that of the intrinsic UO_2 precipitate. Electron DP of the oxidation layer (Figure 2(b)) also shows the characteristic DP of nanocrystalline UO_2, whereas TEM BF image indicates an average grain size of ~300 nm. It is worth mentioning that Si is depleted in the oxidation layer as shown in Figure 2(e). The Si was found to diffuse into the deeper part of the specimen to form a Si-enriched layer (probably USi) between the oxidation layer and the U_3Si_2 matrix (see Mark 2 in Figure 2(a), and Figure 2(f)). This finding is different from the case in the *in situ* TEM ion irradiation investigation, where Si forms a Si-enriched amorphous phase [7]. This difference may be explained as follows: in the *in situ* irradiated TEM foil, the specimen is essentially two-dimensional so that Si atoms cannot diffuse to anywhere else due to the limited geometry. The present observation on high-energy irradiated U_3Si_2 sample unveils a possible oxidation mechanism of the fuel under irradiation.

3.2. The Bubble Region

As predicted by the SRIM simulation (Figure 1(b)), Xe bubbles were observed in a narrow region beyond the UO_2 precipitate. The microstructure features of this bubble region are shown in Figure 3. Three grains can be identified (see G1 through G3 in Figure 3(a)). According to electron DPs (Figure 3(e) and (f)), both G1 and G2 are U_3Si_2. It is noticeable that the irradiation damage is so severe in this region that forbidden reflections of U_3Si_2, such as {101}, {100}, and {031}, appear in the DPs. Due to the limited volume fraction, the electron DP of G3 was challenging to obtain. However, by comparing the EDS profile of G3 with those of G1 and G2 (Figure 3(b) through (d)), G3 has the same element composition as G1 and G2 do, indicating that G3 is also a U_3Si_2 grain. Thus, high-angle grain boundaries can be located as marked by red dashed lines in Figure 3(a). The misorientation of the G1/G2 grain boundary was determined to be 43.1° according to the electron DPs and TEM tilting angles, while the misorientations of grain boundaries involving G3 could not be accurately measured due to the limited size of G3. Meanwhile, based on its nature as an array of dislocations, a subgrain boundary or low-angle grain boundary was also identified in G1, as indicated by the yellow dashed line in Figure 3(a).

Even in this low-magnification STEM HAADF image, bubbles are already distinguishable on those high-angle grain boundaries and the subgrain boundary. More detailed characterizations of those Xe bubbles will be discussed in the following two subsections.

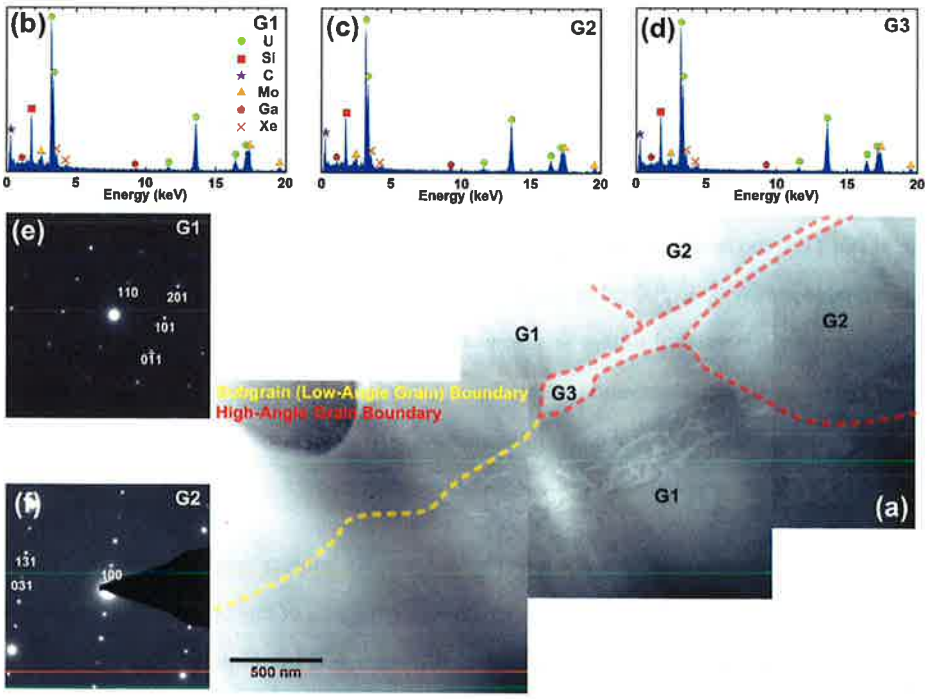

Figure 3: Detailed microstructure of the bubble region: (a) STEM HAADF Z-contrast images of the bubble region, showing both high-angle grain boundaries and a subgrain boundary; (b) through (d) EDS profiles of G1 through G3, showing similar element compositions; (e) and (f) electron diffraction patterns of G1 and G2 showing the characteristic U_3Si_2 patterns.

3.3. Intragranular Bubbles

First, the morphology of intragranular bubbles are concentrated on. Two typical areas in the bubble region were selected to examine intragranular bubbles and are shown as STEM HAADF Z-contrast images (Figure 4(a) and (d)). Both areas are near the subgrain boundary. Aside from the bubbles aggregated on the subgrain boundary, some bubbles were observed to be aligned in several line structures as marked by blue lines in Figure 4(a) and (d). The TEM

BF underfocused images for exactly the same areas (Figure 4(b) and (d)) indicate that those line structures decorated by bubbles are dislocations. No lattice intragranular bubbles can be distinguished in STEM HAADF Z-contrast images, probably due to the high number density and limited size of Xe bubbles. In the TEM BF underfocused images, however, those lattice intragranular bubbles are prominent, especially when the higher magnifications were adopted (Figure 4(c) and (f)). As the spatial distribution of those lattice intragranular bubbles is quite uniform, the number density of them can be straightforwardly measured as 8.5×10^{23} m^{-3}. It is also apparent that intragranular bubbles on dislocations are larger than intragranular bubbles in lattice.

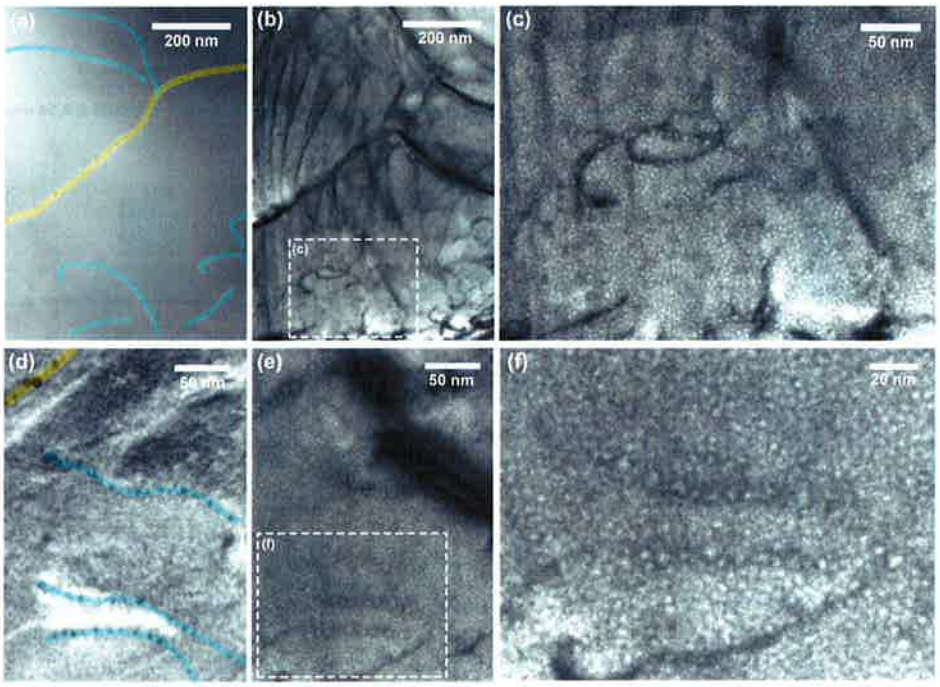

Figure 4: Morphology of intragranular bubbles: (a) and (d) STEM HAADF Z-contrast images of two selected areas in the bubble regions showing the bubbles on dislocations (blue lines) and a subgrain boundary (yellow lines); (b) and (e) TEM BF underfocused images of the same two selected areas showing bubbles on dislocations, on a subgrain boundary, and in lattice; (c) and (f) magnified TEM BF underfocused images of the marked areas in (b) and (e).

A more quantitative comparison was made by measuring the size distributions of intragranular

bubbles in lattice and on dislocations. The size measurement of intragranular bubbles in lattice was performed based on TEM BF underfocused images because those bubbles are not distinguishable in STEM HAADF Z-contrast images. As shown in Figure 5(a), intragranular bubbles in lattice are all smaller than 5 nm in diameter, with an average size of 2.71±0.08 nm. On the other hand, as dislocation bubbles are recognizable in both TEM and STEM images, their size distribution was measured using two imaging techniques respectively, as shown in Figure 5(b) and (c). Both methods give quite similar size distribution: dislocation bubbles are usually larger than lattice bubbles but still smaller than 10 nm; the average size of dislocation bubbles is approximately 4.46±0.15 nm or 4.50±0.14 nm. Dislocations appear to be favored locations for the evolution of intragranular bubbles.

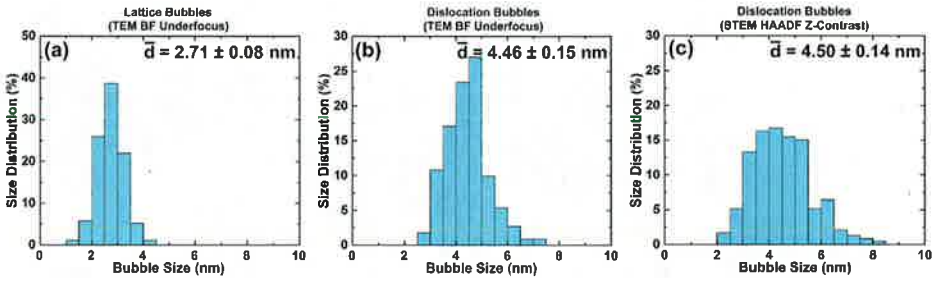

Figure 5: Size distributions of intragranular bubbles measured from TEM/STEM images

3.4. Intergranular Bubbles

The intergranular bubbles have a more complex situation, considering the existence of one subgrain boundary and three high-angle grain boundaries in the bubble region of the TEM foil. In TEM BF underfocused images, while bubbles on the subgrain boundary can still be distinguished due to the similar diffraction contrasts (which originates from similar crystallographic orientations) across the boundary (Figure 4(b) and (e)), bubbles on the high-angle grain boundaries can hardly be recognized as the diffraction contrasts of two grains differ a lot. As a result, only STEM HAADF Z-contrast imaging, which is almost free from diffraction contrast, can be used to investigate intergranular bubbles on the high-angle grain boundaries. As indicated in Figure

6, bubbles on both the subgrain boundary or the high-angle grain boundaries seem larger than bubbles in lattice, which cannot be recognized in STEM HAADF Z-contrast images at all.

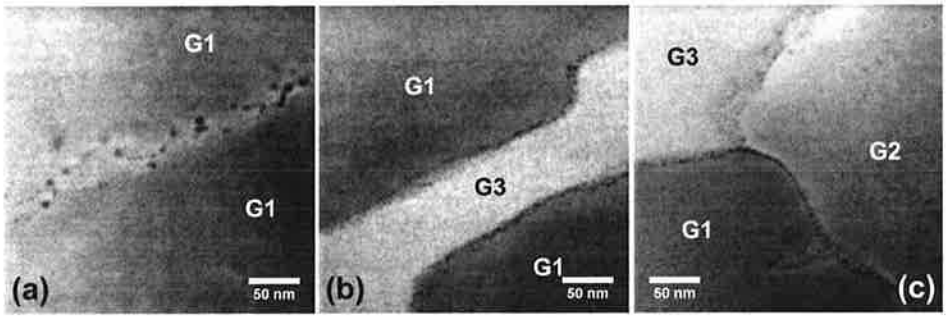

Figure 6: Morphology of intergranular bubbles: (a) a STEM HAADF Z-contrast image showing bubbles on a subgrain boundary; (b) a STEM HAADF Z-contrast image showing bubbles on the high-angle grain boundary between G1 and G3; (c) a STEM HAADF Z-contrast image showing bubbles on the high-angle grain boundary between G1 and G2.

The size distribution of the bubbles on the subgrain boundary was measured using both TEM BF and STEM HAADF images and is shown in Figure 7(a) and (b). Despite that the difference of average subgrain boundary bubble size between two measurement methods is with the margin of error, it still implies that STEM HAADF Z-contrast imaging gives a more accurate subgrain boundary bubble size, because the contrast of small bubbles on the subgrain boundaries can be interfered by the diffraction contrast of the boundary. Additionally, the size distributions of bubbles on the high-angle grain boundaries were also measured using the STEM HAADF images. Since the grain boundary between G2 and G3 is located in a thick area of the TEM foil, the measurement was focused on the G1/G3 and G1/G2 grain boundaries (see Figure 7(c) and (d)). It is also noticeable that average bubble sizes on the two high-angle grain boundaries differ a bit.

4. Discussion

In a previous *in situ* TEM ion irradiation investigation [7], U_3Si_2 was proven to maintain its crystalline structure up to 5 dpa at LWR temperatures. In this high-energy ion implantation study, the peak irradiation damage dose was raised significantly. At 300°C, U_3Si_2 shows its

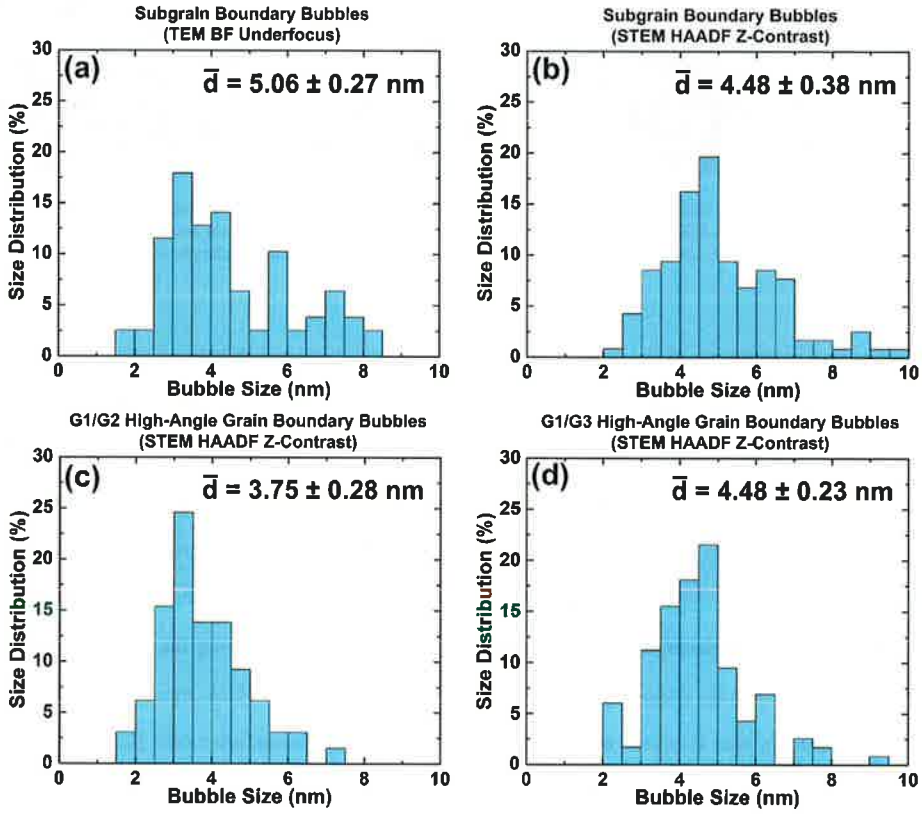

Figure 7: Size distributions of integranular bubbles measured from TEM/STEM images

capability of maintaining crystalline up to approximately 500 dpa. This further demonstrates that amorphization is not a concern for applying U_3Si_2 in LWRs.

The majority of Xe atoms were found to stay in lattice intragranular bubbles, which has a number density of 8.5×10^{23} m^{-3}. This measured number density could still be underestimated considering the overlapping effect of the extremely dense bubble distribution. At 300°C, it seems that thermally-activated diffusion of Xe is still insufficient to initiate bubble coalescence that induces larger lattice intragranular bubbles.

As previous reported [7, 25], dislocation density is low in U_3Si_2 pellet prior to irradiation. Hence, the dislocations observed in the bubble region were induced by ion irradiation. As local sources of stress field, dislocations are strong sinks for both point defects and impurity atoms (e.g. Xe atoms) and therefore are potential aggregation sites for Xe bubbles. In fact, in irradiated materials, it was reported that voids or He bubbles preferentially nucleate and grow on dislocations [26, 27]. Inspired by this kind of observations, it was assumed that dislocation bubbles are a special type of intragranular bubbles that need to be separately analyzed in fuel performance codes [28, 29]. However, although fission gas bubbles were found to form in lines in UO_2 [30, 31, 32], few confirmed observations of bubble decoration on dislocations have been reported in nuclear fuels. In this study, Xe bubble decoration on dislocations was directly observed. More importantly, intragranular bubbles on dislocations have a deterministically larger size compared to lattice intragranular bubbles, which confirms the long-standing assumption [28, 29]. More importantly, the 499 dpa peak damage dose in this study only corresponds to U_3Si_2 fuel with ~1%FIMA. In an in-pile irradiated fuel pellet with over 5%FIMA, the higher irradiation damage is expected to create much denser dislocations, which may further facilitate the nucleation and growth of intragranular bubbles on dislocations.

As mentioned before, the nature of a subgrain boundary, which is also known as a low-angle grain boundary, is an array of dislocations. Considering the subgrain boundary observed in this study is located in the high irradiation dose region that is filled with radiation-induced dislocations, the formation of the subgrain boundary may originate from the accumulation of irradiation-induced dislocations. This irradiation-induced evolution mechanism of subgrain boundaries

may further lead to grain subdivision and formation of high-burnup structure (HBS) as radiation dose continues to increase. Ion irradiation experiments involving higher doses need to be conducted to confirm the threshold dose of grain subdivision. As an array of dislocations, the subgrain boundary also behaves as a sink for defects and impurities and thus has preferential bubble evolution on it. Because a subgrain boundary is still composed of dislocations, the size distribution of subgrain boundary bubbles is similar to that of intragranular bubbles on dislocations as expected.

Unlike a subgrain boundary, a high-angle grain boundary is an interface of two domains with dissimilar crystallographic orientations. High-angle grain boundaries are also sinks for defects and impurities so that Xe bubbles were also found to aggregate on them. It is interesting that among the two high-angle grain boundaries investigated in this study, a prominent difference can be found in their size distribution. This implies that high-angle grain boundaries of various types (tilt, twist, and mixed, etc.) and Σs may have different sink strengths and therefore different kinetics for intergranular bubble evolution.

Although the bubbles on dislocations, subgrain boundaries, and high-angle grain boundaries are all lager than intragranular bubbles in lattice, all the bubbles are smaller than 10 nm, which is quite small compared to bubbles observed in other nuclear fuels [20]. In addition, none bubble interconnection or bubble channel formation was found in the Xe-implanted specimen. Therefore, according to this study, at 300°C, Xe gas atoms of concentration equivalent to a ~6%FIMA can be retained in U_3Si_2 with a limited swelling strain, which demonstrate the excellent fission gas behavior of U_3Si_2. As a accelerated irradiation experiment powered by high-energy Xe ions, this study involves a higher irradiation dose rate and a shorter annealing time in comparison to in-pile irradiation conditions. As a result, the hgih-energy Xe implantation in this study might not replicate the exact microstructure modifications in U_3Si_2 as in-pile neutron irradiation does. However, by using the similar temperature, fission fragment energy, and Xe fraction conditions, it is believed that this study is capable of providing some qualitative results of fission gas behavior in U_3Si_2 under LWR conditions so as to guide the modeling and experimental efforts on U_3Si_2 fuel performance study before the availability of the PIE data of the in-pile irradiation campaign.

5. Conclusions

In summary, 84 MeV Xe ions was utilized to irradiate a U_3Si_2 specimen at 300°C to study the fission gas behavior of U_3Si_2 at LWR temperatures. TEM/STEM investigations unveil the formation of dense distribution of small lattice intragranular bubbles. Xe ion irradiation also creates a great number of dislocations in the specimen, some of which may even accumulate into a subgrain boundaries. Xe bubbles with a slightly larger size were found on those irradiation-induced dislocations/subgrain boundaries as well as the preexistent high-angle grain boundaries. All the implanted Xe was retained within the U_3Si_2 without any observable gas release issue. The high-energy Xe implantation experiments proved to provide comprehensive information of fission gas behavior in U_3Si_2 at a typical LWR temperature, which can be valuable references for the fuel performance research of U_3Si_2 as an ATF candidate.

6. Acknowledgments

This work was funded by the Accident Tolerant Fuel High-Impact Problems (ATF HIP) of the U.S. Department of Energy (DOE)'s Nuclear Energy Advanced Modeling and Simulation (NEAMS) program. The authors would also like to acknowledge the help of Matthew Hendricks on the ATLAS irradiation. This research used resources of Argonne National Laboratorys ATLAS facility, which is a DOE Office of Science User Facility. The efforts involving Argonne National Laboratory were sponsored under Contract no. DE-AC02-06CH11357 between UChicago Argonne, LLC and the U.S. Department of Energy. This work was supported by the U.S. Department of Energy, Office of Nuclear Energy under DOE Idaho Operations Office Contract DE-AC07-051D14517 as part of a Nuclear Science User Facilities experiment.

Fabrication of the samples used in this work was supported by the U.S. Department of Energy, Office of Nuclear Energy. Fabrication was part of a collaboration led by Westinghouse Electric Company comprising several national laboratories, vendors, and universities awarded in response to the DE-FOA-0001063 funding opportunity. The authors would like to acknowledge the assistance of the support staff associated with the Fuels Applied Science Building at Idaho National Laboratory specifically Rita Hoggan for preparing samples for ion irradiation.

References

[1] J. Carmack, F. Goldner, S. M. Bragg-Sitton, L. L. Snead, in: Proc. 2013 LWR Fuel Performance Meeting/TopFuel 2013, pp. 15–19.

[2] S. J. Zinkle, K. A. Terrani, J. C. Gehin, L. J. Ott, L. L. Snead, Journal of Nuclear Materials 448 (2014) 374–379.

[3] J. White, A. Nelson, J. Dunwoody, D. Byler, D. Safarik, K. McClellan, Journal of Nuclear Materials 464 (2015) 275–280.

[4] K. Metzger, T. Knight, R. Williamson, in: Proceedings of the International Congress on Advances in Nuclear Power Plants–ICAPP 2014, Charlotte, NC.

[5] J. M. Harp, P. A. Lessing, R. E. Hoggan, Journal of Nuclear Materials 466 (2015) 728–738.

[6] S. Middleburgh, R. Grimes, E. Lahoda, C. Stanek, D. Andersson, Journal of Nuclear Materials 482 (2016) 300–305.

[7] Y. Miao, J. Harp, K. Mo, S. Bhattacharya, P. Baldo, A. M. Yacout, Journal of Nuclear Materials 484 (2017) 168–173.

[8] L. He, J. M. Harp, R. E. Hoggan, A. R. Wagner, Journal of Nuclear Materials 486 (2017) 274–282.

[9] G. L. Hofman, Journal of Nuclear Materials 140 (1986) 256–263.

[10] A. Leenaers, S. Van den Berghe, E. Koonen, P. Jacquet, C. Jarousse, B. Guigon, A. Ballagny, L. Sannen, Journal of nuclear materials 327 (2004) 121–129.

[11] M. Finlay, G. Hofman, J. Snelgrove, Journal of nuclear materials 325 (2004) 118–128.

[12] G. L. Hofman, Y. S. Kim, Nuclear Engineering and Technology 37 (2005) 299–308.

[13] Y. S. Kim, G. Hofman, J. Rest, A. Robinson, Journal of Nuclear Materials 389 (2009) 443–449.

[14] R. Birtcher, J. Richardson, M. Mueller, Journal of nuclear materials 230 (1996) 158–163.

[15] J. M. Harp, Personal communication, 2017. Idaho National Laboratory.

[16] J. Carmack, K. Barrett, H. MacLean-Chichester, Light Water Reactor Accident Tolerant Fuels Irradiation Testing, Technical Report, Idaho National Laboratory (INL), Idaho Falls, ID (United States), 2015.

[17] R. Averback, R. Benedek, K. Merkle, Journal of Nuclear Materials 75 (1978) 162–166.

[18] C. Abromeit, Journal of nuclear materials 216 (1994) 78–96.

[19] G. S. Was, Journal of Materials Research 30 (2015) 1158–1182.

[20] B. Ye, L. Jamison, Y. Miao, S. Bhattacharya, G. Hofman, A. Yacout, Journal of Nuclear Materials 488 (2017) 134–142.

[21] M. Pellin, A. M. Yacout, K. Mo, J. Almer, S. Bhattacharya, W. Mohamed, D. Seidman, B. Ye, D. Yun, R. Xu, et al., Journal of Nuclear Materials 471 (2016) 266–271.

[22] J. F. Ziegler, M. D. Ziegler, J. P. Biersack, Nuclear Instruments and Methods in Physics Research Section B: Beam Interactions with Materials and Atoms 268 (2010) 1818–1823.

[23] R. E. Stoller, M. B. Toloczko, G. S. Was, A. G. Certain, S. Dwaraknath, F. A. Garner, Nuclear instruments and methods in physics research section B: beam interactions with materials and atoms 310 (2013) 75–80.

[24] J. Blanchard, D. Butt, M. Meyer, P. Xu, Development of Advanced High Uranium Density Fuels for Light Water

Reactors, Technical Report Project No. 11-3041, U.S. Department of Energy Nuclear Energy University Programs (NEUP) Final Report, 2016.

[25] Y. Miao, K. Mo, A. Yacout, J. Harp, Simulated Fission Gas Behavior in Silicide Fuel at LWR Conditions, Technical Report, Argonne National Laboratory (ANL), 2016.

[26] S. Amelinckx, W. Maenhout-Van der Vorst, W. Dekeyser, Acta Metallurgica 7 (1959) 8–17.

[27] B. N. Singh, T. Leffers, W. Green, M. Victoria, Journal of Nuclear Materials 125 (1984) 287–297.

[28] G. Greenwood, A. Foreman, D. Rimmer, Journal of Nuclear Materials 1 (1959) 305–324.

[29] J. Rest, GRASS-SST: a comprehensive, mechanistic model for the prediction of fission-gas behavior in UO/sub 2/-base fuels during steady-state and transient conditions, Technical Report, Argonne National Lab., IL (USA), 1978.

[30] J. Turnbull, Journal of Nuclear Materials 38 (1971) 203–212.

[31] R. Cornell, Journal of Nuclear Materials 38 (1971) 319–328.

[32] C. Baker, Journal of Nuclear Materials 66 (1977) 283–291.